

Soft-switching Converter for Inductive Power Transfer System with Double-sided LCC Resonant Network

Ryohei Okada^{1*}, Ryosuke Ota*, Nobukazu Hoshi*

*Tokyo University of Science

2641 Yamazaki Noda-city

Chiba, Japan

Email: ¹r_okada@alumni.tus.ac.jp

Keywords

«Wireless power transmission», «Electric vehicle», «Soft switching», «ZVS converters»,
«Bi-directional»

Abstract

In a general soft switching method for inductive power transfer (IPT) systems, a reactive current is intentionally generated in the resonant network and then utilized to achieve soft switching. However, the whole-system efficiency worsens because the reactive current circulates in the system. Against this problem, the soft-switching active bridge (SAB) converter is proposed. The SAB converter comprises the full-bridge active converter and the LC circuit, which can generate the reactive current in place of the resonant network. As a result, the reactive current circulating in the system is reduced, and high efficiency can be achieved. This paper shows how to apply the SAB converter to IPT systems with the double-sided LCC topology. The theoretical analysis clarifies the effect of the design of the LC circuit on the whole-system efficiency, and the design guideline for the LC circuit is discussed. In the experiment, the validities of the theoretical analysis result and the design guideline are shown. The SAB-IPT system can get higher efficiency over wide operation range as well as the theoretical analysis result. Especially, the efficiency at 2.5 kW-output is improved by 0.69 points, and the efficiency at 1.5 kW-output is improved by 0.88 points.

Introduction

Recently, as a means to dramatically extend the driving range of electric vehicles (EVs), inductive power transfer (IPT) technology is expected [1–4]. Currently, the IPT system is required to increase power for rapid charging. However, we have challenges regarding the increase in power loss in the system and switching noise from the semiconductor devices.

Soft switching is a technique to reduce the electromagnetic noise and the loss caused by switching. In a general soft switching method for IPT systems, a reactive current is intentionally generated in the resonant network and then utilized to achieve soft switching [5–7]. However, it has been indicated that the whole-system efficiency is significantly worsened in some operation points [5–9]. The reason is that the reactive current generated in the resonant network circulates in the system. As a result, its conduction loss significantly influences efficiency, especially in the operation points where the reactive current is large. In other words, there is a trade-off relationship between switching-noise reduction and efficiency improvement. To solve this problem, a method where the reactive current is alternatively generated by the LC circuit added to the full-bridge active (FBA) converter has been proposed [10]. The reactive current generated by the LC circuit does not circulate in the whole system. In addition, the resonant

network, which has large ESRs, does not need to generate a large reactive current due to the LC circuit. As a result, the proposed method can largely reduce the total conduction loss in the whole system.

In the literature [10], the effectiveness of the FBA converter with the LC circuit, which is called the soft switching active bridge (SAB) converter, is clarified for IPT systems with the series/series (SS) compensation resonant network. However, there are various compensation topologies for the resonant network. These input-impedance characteristics and behaviors of the coupling change between the transmission coils are different. Especially in charging in-motion, such as dynamic IPT systems for EVs, the double-sided LCC topology shown in Fig. 1 could be a better choice than the SS topology [5, 11, 12]. Therefore, it is necessary to clarify how to apply the SAB converter to the double-sided LCC resonant network and its effectiveness.

Against this background, this paper clarifies the operation method, the design guideline, and the effectiveness of the SAB-IPT system shown in Fig. 1. This paper discusses these with the theoretical analysis and the experiment compared with the conventional FBA-IPT system. In this paper, the IPT system comprising the FBA converters is called “FBA-IPT system”, and the IPT system comprising the SAB converters is called “SAB-IPT system”.

System Overview

System Configuration

The system shown in Fig. 1 comprises a double-sided LCC resonant network and the SAB converters on the primary/secondary sides. In a SAB converter, one LC circuit is connected to one-side leg of the general FBA converter. Moreover, the LC circuits comprise the inductors L_{LCp} , L_{LCS} to generate the reactive current and the capacitors C_{LCp} , C_{LCS} , which absorb the DC components of the voltages on S_{p4} , S_{s2} . The DC-bus voltages on both SAB converters are constant, and the AC-side voltages on the SAB converters are regulated with phase-shift control between the legs. Then, the duty ratio of each switch is fixed to 0.5, and the switching frequency is fixed to 85 kHz. In addition, the amount of the reactive current in the resonant network can be regulated with phase-shift control between the primary and secondary sides.

Power Transfer in SAB-IPT System with Double-sided LCC Resonant Network

Fig. 2 shows the operation waveforms in the primary-side SAB converter. Since the operation waveforms in the secondary side can be drawn as well as the primary side, these descriptions are omitted. From Fig. 2, the phasor notation for fundamental components \dot{V}_{p1} , \dot{V}_{s1} [V] of the

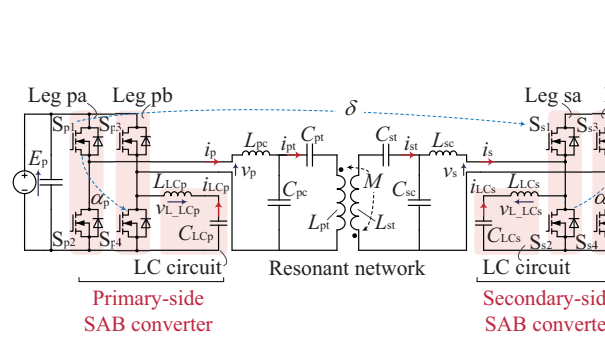


Fig. 1: SAB-IPT system with the double-sided LCC resonant network.

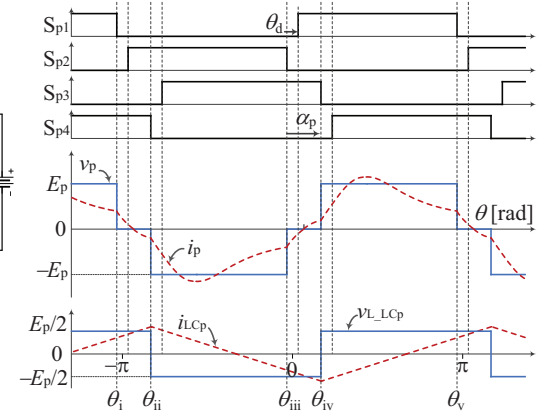


Fig. 2: Operation waveforms in the primary-side SAB converter.

output/input voltages on the primary/secondary-sides SAB converters are expressed as

$$\dot{V}_{p1} = \frac{2\sqrt{2}E_p}{\pi} \cos \frac{\alpha_p}{2} \varepsilon^{j(-\alpha_p/2 + \theta_d/2)}, \quad \dot{V}_{s1} = \frac{2\sqrt{2}E_s}{\pi} \cos \frac{\alpha_s}{2} \varepsilon^{j(\delta - \alpha_s/2 + \theta_d/2)}, \quad (1)$$

where E_p [V] represents the primary-side DC voltage, and E_s [V] represents the battery voltage. α_p and α_s [rad] represent the phase-shift angles between the legs in the primary/secondary-side converters, respectively. Additionally, δ [rad] denotes the phase-shift angle between the primary/secondary-side SAB converters, and θ_d [rad] represents the dead-time converted to the angle. For simplicity, this chapter does not consider the harmonic components of each voltage. When ESRs of each element are ignored and the switching angular frequency of both converters matches the resonant angular frequency ω in the resonant network, the phasor notation for fundamental components \dot{I}_{p1} and \dot{I}_{s1} [A] of the output/input currents on the primary/secondary SAB converters are respectively expressed as [5, 11]

$$\dot{I}_{p1} = \frac{M\dot{V}_{s1}}{j\omega L_{pc}L_{sc}}, \quad \dot{I}_{s1} = \frac{M\dot{V}_{p1}}{j\omega L_{pc}L_{sc}}, \quad (2)$$

where L_{pc} and L_{sc} [H] represent the compensation inductors, and M [H] represents the mutual inductance between the transmission coils L_{pt} and L_{st} [H]. Moreover, the phasor notation for fundamental components \dot{I}_{pt1} and \dot{I}_{st1} [A] of the currents flowing in the transmission coils L_{pt} and L_{st} can be respectively expressed as

$$\dot{I}_{pt1} = \frac{\dot{V}_{p1}}{j\omega L_{pc}}, \quad \dot{I}_{st1} = \frac{\dot{V}_{s1}}{j\omega L_{sc}}. \quad (3)$$

Then, the transmission power P_{tr} [W] of the resonant network is given by [11]

$$P_{tr} = \frac{M|\dot{V}_{p1}||\dot{V}_{s1}|}{\omega L_{pc}L_{sc}} \cos \phi \quad \left(\phi = \frac{\pi}{2} - \theta_{vps} \right), \quad (4)$$

where $\cos \phi$ represents the displacement factor in the resonant network, and ϕ can be controlled with the phase-shift angle θ_{vps} [rad] between \dot{V}_{p1} and \dot{V}_{s1} . In this paper, the resonant-network efficiency η_{rn} [%] is defined as [5]

$$\eta_{rn} = \frac{100P_{tr}}{P_{tr} + r_{Lpc}|\dot{I}_{p1}|^2 + r_{pt}|\dot{I}_{pt1}|^2 + r_{st}|\dot{I}_{st1}|^2 + r_{Lsc}|\dot{I}_{s1}|^2}, \quad (5)$$

where r_{Lpc} and r_{Lsc} [Ω] represent the ESRs in L_{pc} and L_{sc} , respectively. In addition, r_{pt} , r_{st} [Ω] represent the total ESRs in L_{pt} and C_{pt} , L_{st} and C_{st} , respectively. The equation (5) does not consider the conduction losses in the compensation capacitors C_{pc} and C_{sc} [F].

Here, by substituting the equations (2)–(4) into (5), η_{rn} can be expressed as

$$\eta_{rn} = \frac{100}{1 + \frac{\left| \frac{\dot{V}_{s1}}{\dot{V}_{p1}} \right| \left(r_{Lpc} + r_{st} \frac{L_{pc}^2}{M^2} \right) + \left| \frac{\dot{V}_{p1}}{\dot{V}_{s1}} \right| \left(r_{Lsc} + r_{pt} \frac{L_{sc}^2}{M^2} \right)}{\frac{M}{\omega L_{pc}L_{sc}} \cos \phi}}. \quad (6)$$

From the denominator of (6), the requirements for the maximum efficiency of the resonant network can be derived by using the relationship of the arithmetic-geometric mean [6, 7]. As a result, these requirements can be expressed as

$$\begin{cases} \frac{|\dot{V}_{s1}|^2}{|\dot{V}_{p1}|^2} = \frac{|\dot{I}_{p1}|^2}{|\dot{I}_{s1}|^2} = \frac{r_{pt}L_{sc}^2 + r_{Lsc}M^2}{r_{st}L_{pc}^2 + r_{Lpc}M^2}, \\ \phi = 0. \end{cases} \quad (7)$$

$$(8)$$

Moreover, (7) can be transformed to

$$r_{Lsc}|\dot{I}_{s1}|^2 + r_{pt}|\dot{I}_{pt1}|^2 = r_{Lpc}|\dot{I}_{p1}|^2 + r_{st}|\dot{I}_{st1}|^2, \quad (9)$$

where the left hand side represents the losses regarding \dot{V}_{p1} and the right hand side represents the losses regarding \dot{V}_{s1} . In other words, the requirement means that the power losses regarding \dot{V}_{p1} and \dot{V}_{s1} need to be balanced. On the other hand, (8) means the requirement where the displacement factor of the resonant network becomes a unity. In other words, the fundamental component of the reactive current in the resonant network is minimized with (8). Thus, when (7) and (8) are satisfied, the resonant network gets high efficiency.

Operation Modes of SAB Converter

This chapter explains the overview of the operation modes of the SAB converter based on the literature [10]. This chapter omits the detailed operation modes because it is explained in [10]. Fig. 3 shows the operation modes of the primary-side SAB converter whose waveforms correspond to Fig. 2. The dead-time period is omitted for simplicity. The operation of the secondary-side SAB converter is not explained because we can explain it as well as that of the primary side.

The operation of the SAB converter can be explained by superimposing the operations of the LC circuit and the resonant network. Therefore, each operation is explained.

Operation Mode of LC circuit

The operation mode of the LC circuit depends on the operation of the Leg pb in Fig. 3. When the duty ratios of the switches are set to 0.5, the waveforms of the voltage v_{LCp} [V] and the current i_{LCp} [A] are represented as shown in Fig. 2. In this case, the currents i_{LCp} , i_{LCs} [A] flowing in the LC circuits are expressed as

$$i_{LCp} \simeq \sum_{n=1}^m \frac{1}{n^2 \pi \omega L_{LCp}} 2E_p \sin \frac{n\pi}{2} \sin \left\{ n \left(\theta - \alpha_p + \frac{\theta_d}{2} - \frac{\pi}{2} \right) \right\}, \quad (10)$$

$$i_{LCs} \simeq \sum_{n=1}^m \frac{1}{n^2 \pi \omega L_{LCs}} 2E_s \sin \frac{n\pi}{2} \sin \left\{ n \left(\theta - \frac{\alpha_p - \alpha_s - 2\theta_{vps}}{2} + \frac{\theta_d}{2} + \frac{\pi}{2} \right) \right\}. \quad (11)$$

In this paper, $m = 5$ is assumed.

Operation Mode of Resonant Network

The resonant network is driven by the four operation modes shown in Fig. 3 as well as when the general FBA-IPT system is connected to it. In this paper, the only phase-shift angle between the legs is controlled, and the duty ratios of all switches are set to 0.5 constantly.

The resonant-network currents i_p and i_s , which consider harmonics, are derived by

$$i_p \simeq \sum_{n=1}^l \sqrt{2} I_{pn_rms} \sin(n\theta + \theta_{ipn}), \quad (12)$$

$$i_s \simeq \sum_{n=1}^l \sqrt{2} I_{sn_rms} \sin(n\theta + \theta_{isn}), \quad (13)$$

where the RMS values I_{pn_rms} and I_{sn_rms} [A] of harmonic components of these currents are shown in Table I. In addition, θ_{ipn} and θ_{isn} [rad] represent the phase angles of \dot{I}_{pn} and \dot{I}_{sn} . In this paper, $l = 7$ is assumed.

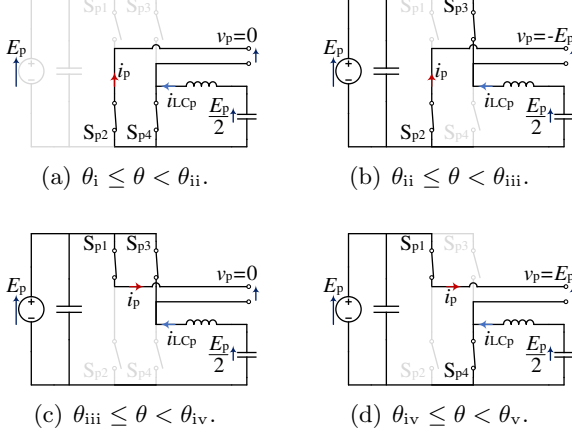


Fig. 3: Operation modes of the primary-side SAB converter.

Table I: Detail of variables related to I_{pn_rms} and I_{sn_rms}

I_{pn_rms}	$\left \frac{(\dot{x}_b \dot{x}_c \dot{x}_d - \dot{x}_b \dot{x}_g^2 - \dot{x}_d \dot{x}_f^2) \dot{V}_{pn} + \dot{x}_e \dot{x}_f \dot{x}_g \dot{V}_{sn}}{\dot{x}_a (\dot{x}_b \dot{x}_c \dot{x}_d - \dot{x}_b \dot{x}_g^2 - \dot{x}_d \dot{x}_f^2) - \dot{x}_e^2 (\dot{x}_c \dot{x}_d - \dot{x}_g^2)} \right $
I_{sn_rms}	$\left \frac{-\dot{x}_e \dot{x}_f \dot{x}_g \dot{V}_{pn} + (\dot{x}_c \dot{x}_e^2 + \dot{x}_a \dot{x}_f^2 - \dot{x}_a \dot{x}_b \dot{x}_c) \dot{V}_{sn}}{\dot{x}_a (\dot{x}_b \dot{x}_c \dot{x}_d - \dot{x}_b \dot{x}_g^2 - \dot{x}_d \dot{x}_f^2) - \dot{x}_e^2 (\dot{x}_c \dot{x}_d - \dot{x}_g^2)} \right $
\dot{V}_{pn}	$\frac{2\sqrt{2}E_p}{n\pi} \cos \frac{n\alpha_p}{2} \varepsilon^{jn} \left(-\frac{\alpha_p}{2} + \frac{\theta_d}{2} \right)$
\dot{V}_{sn}	$\frac{2\sqrt{2}E_s}{n\pi} \cos \frac{n\alpha_s}{2} \varepsilon^{jn} \left(\delta - \frac{\alpha_s}{2} + \frac{\theta_d}{2} \right)$
\dot{x}_a	$j n \omega L_{pc} + \frac{1}{j n \omega C_{pc}}$
\dot{x}_b	$j n \omega L_{pt} + \frac{1}{j n \omega C_{pt}} + \frac{1}{j n \omega C_{pc}}$
\dot{x}_c	$j n \omega L_{st} + \frac{1}{j n \omega C_{st}} + \frac{1}{j n \omega C_{sc}}$
\dot{x}_d	$j n \omega L_{sc} + \frac{1}{j n \omega C_{sc}}$
\dot{x}_e	$\frac{-1}{j n \omega C_{pc}}$
\dot{x}_f	$-j n \omega M$
\dot{x}_g	$\frac{-1}{j n \omega C_{sc}}$

Soft-switching Requirement

This chapter describes the soft-switching requirement for SAB converter and the method to achieve soft switching. The type of soft switching is divided into soft-switching turn-off and -on. However, the detail of the requirement for the soft switching turn-off is not explained. This reason is that the parasitic D-S capacitance works so as to prevent the rapid voltage rising when the switching device turns off [13]. Therefore, this paper assumes that the soft-switching turn-off is always achieved.

On the other hand, a switch can turn on with soft switching by discharging the charge in the D-S parasitic capacitor during the dead-time period before the turn-on. Then, the requirements for soft switching in the primary-side SAB converter are shown in the following.

$$\begin{cases} i_p (-\theta_d/2) \leq 0 & i_p (\alpha_p - \theta_d/2) + i_{LCp} (\alpha_p - \theta_d/2) \leq 0 \\ i_p (\theta_d/2) \leq 0, & i_p (\alpha_p + \theta_d/2) + i_{LCp} (\alpha_p + \theta_d/2) \leq 0, \end{cases} \quad (14)$$

where the left-side condition represents the soft-switching requirement for Leg pa, and the right-side condition represents the soft-switching requirement for Leg pb. In addition, the requirements for soft switching in the secondary-side SAB converter are shown in the following.

$$\begin{cases} i_s (-\delta - \theta_d/2) + i_{Lcs} (-\delta - \theta_d/2) \geq 0 & i_s (-\delta + \alpha_s - \theta_d/2) \geq 0 \\ i_s (-\delta + \theta_d/2) + i_{Lcs} (-\delta + \theta_d/2) \geq 0, & i_s (-\delta + \alpha_s + \theta_d/2) \geq 0, \end{cases} \quad (15)$$

where the left-side condition represents the soft-switching requirement for Leg sa, and the right-side condition represents the soft-switching requirement for Leg sb. In the requirement for the legs, the term regarding the currents i_{LCp} and i_{Lcs} in the LC circuits is contained. Thus, the SAB converter can also utilize the LC circuit current for soft switching. Therefore, the degree of freedom of i_p and i_s increases while achieving soft switching, and the resonant network can be driven with a near unity displacement factor. As a result, the high efficient operation area can be expanded.

However, the conduction loss by i_{LCp} and i_{Lcs} cannot be ignored when i_{LCp} and i_{Lcs} are large. Therefore, we need to design the LC circuit considering the balance between the degree of freedom and the conduction losses. In the next chapter, the effect of the LC circuit on the

whole-system efficiency is analyzed. In addition, a design guideline for the LC circuit is discussed.

Efficiency Analysis of SAB-IPT System with Double-sided LCC Resonant Network

In this chapter, the effect of the LC circuit design on the whole-system efficiency is clarified based on the theoretical analysis. In this analysis, the circuit parameters shown in Table II are used. This paper analyzes under the condition $L_{LC_p} = L_{LC_s} = L_{LC}$ for simplicity.

Definition of Whole System Efficiency

Here, the whole-system efficiency η [%] in the soft-switching operation is defined as

$$\eta = \frac{100P_{tr}}{P_{tr} + P_{rn} + P_{sw_con} + P_{sw_turn\ off} + P_{LC}}, \quad (16)$$

where P_{rn} [W] represents the total conduction loss in the resonant network, and P_{LC} [W] represents the total conduction loss of the LC circuits. In addition, P_{sw_con} and $P_{sw_turn\ off}$ [W] represent the total conduction loss and the total turn-off loss in all switches, respectively. These losses are calculated based on the calculation method shown in [10].

Analysis of Relationship between L_{LC} and Whole-System Efficiency

Fig. 4 shows the theoretical maximum-efficiency characteristics of the whole system at $P_{tr} = 2.5$ kW when L_{LC} is varied so as to satisfy the soft switching requirement. The characteristics of $\eta_{max}(L_{LC})$ are exhaustively explored from sets of α_p , α_s and ϕ with satisfying the following equation.

$$\cos \frac{\alpha_p}{2} \cos \frac{\alpha_s}{2} \cos \phi = \frac{\pi^2 \omega L_{pc} L_{sc}}{8 M E_p E_s} P_{tr}^*, \quad (17)$$

where P_{tr}^* represents the rated power. In Fig. 4, when $L_{LC} > L_{LC_max}$, i_{LC_p} and i_{LC_s} are small. In other words, in order to satisfy (14) and (15), we need to use the help of the reactive current from the resonant network. However, when $L_{LC} \leq L_{LC_max}$, i_{LC_p} and i_{LC_s} are large. As a result, (14) and (15) are satisfied without the reactive current of the resonant network. As a result, the high-efficiency condition (8) of the resonant network can be satisfied. In addition, the whole-system efficiency is maximized when $L_{LC} = L_{LC_max}$, i_{LC_p} and i_{LC_s} are minimized. However, it is confirmed that L_{LC_max} varies depending on the coupling coefficient from Fig. 4.

Table II: Circuit parameters in the experimental system

Coupling coefficient k between L_{pt} and L_{st}	0.2, 0.3
Primary/Secondary-sides DC voltages E_p , E_s	240 V
Switching frequency in each converter f	85 kHz
Transmission coils L_{pt} , L_{st}	62.1, 69.0 μ H
Compensation inductor L_{pc} , L_{sc}	17.1, 22.9 μ H
Inductors in the LC circuits L_{LC_p} , L_{LC_s}	20.0, 34.0 μ H
Switching devices	ROHM BSM080D12P2C008

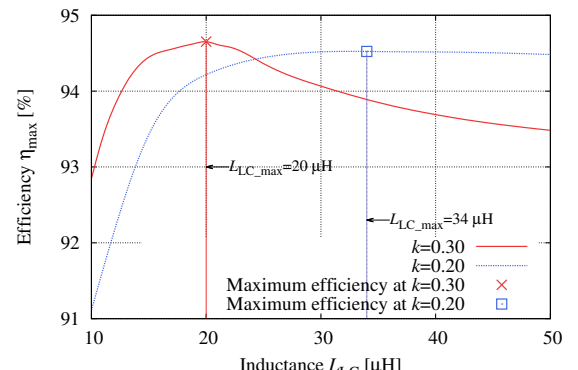


Fig. 4: Theoretical maximum-efficiency characteristics of the whole system at $P_{tr} = 2.5$ kW when L_{LC} is varied so as to satisfy the soft-switching requirement.

This is due to the following reasons. From (4), larger coupling coefficient k results in larger transmission power P_{tr} . Then, in order to keep P_{tr} constant, v_p and v_s need to be controlled to smaller values by increasing α_p and α_s . When α_p and α_s are large, the current values of i_p and i_s at switching are also large in the one-side leg. In other words, a larger current is needed for soft switching in this case. From the above, it can be said the larger k brings the smaller $L_{\text{LC_max}}$.

From the above characteristics, it is preferable to make L_{LC} small for a system where it is not difficult to maintain close coupling of the coils. On the other hand, it is preferable to make L_{LC} large for a system where it is difficult to maintain close coupling of the coils such as a dynamic IPT system. In the next section, the validity of the theoretical analysis result is evaluated by using two inductors L_{LC} ($20.0, 34.0 \mu\text{H}$). A detailed discussion of the design method for the LC circuit will be reported in the future.

Comparison between FBA-IPT System and SAB-IPT System

This chapter compares the power losses and the efficiencies of the FBA-IPT/SAB-IPT systems in a theoretical analysis. In addition, its validity is shown by experimental results. The analysis and the experiment are conducted based on the parameters shown in Table II. Through the comparison, it is confirmed that the effectiveness of the SAB-IPT system to which the double-sided LCC is connected.

Theoretical Analysis

Fig. 5 shows the whole-system efficiency based on the theoretical analysis ($k = 0.3$). The soft-switching operation area is only drawn in Fig. 5. The line on the rim of the operation represents the maximum efficiency points for each transmission power. From Fig. 5, it can be confirmed that the soft-switching operation area of the SAB-IPT system expands compared with that of the FBA-IPT system. In other words, as mentioned in the previous chapter, the degree of freedom of θ_{vps} increases, and then the SAB-IPT system can be operated with $\theta_{\text{vps}} = \pi/2$ ($\cos \phi = 1$) at $L_{\text{LC}} = 20.0 \mu\text{H}$. Additionally, the SAB-IPT system can be operated with a higher displacement factor than the FBA-IPT system even at $L_{\text{LC}} = 34.0 \mu\text{H}$. As a result, the whole-system efficiency is also improved.

Here, Fig. 6 shows the maximum efficiency characteristics of FBA/SAB-IPT systems controlled according to Fig. 5. From Fig. 6, it can be confirmed that the SAB-IPT system achieves higher efficiency than the FBA-IPT system over wide operation range. Here, Fig. 7 shows the power-loss breakdown based on the theoretical analysis at $k = 0.2$. From Fig. 7, it can be confirmed that each power loss except for P_{LC} in the SAB-IPT system is smaller than that in the FBA-IPT

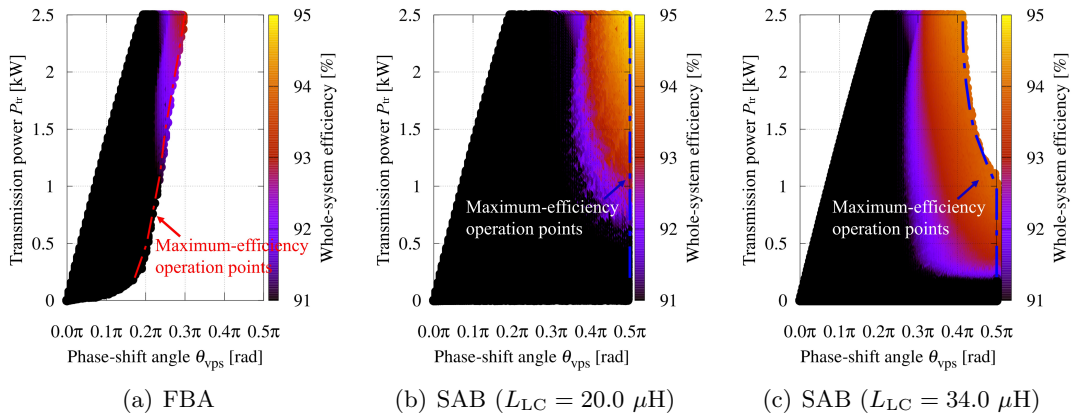


Fig. 5: Whole-system efficiency based on the theoretical analysis ($k = 0.3$).

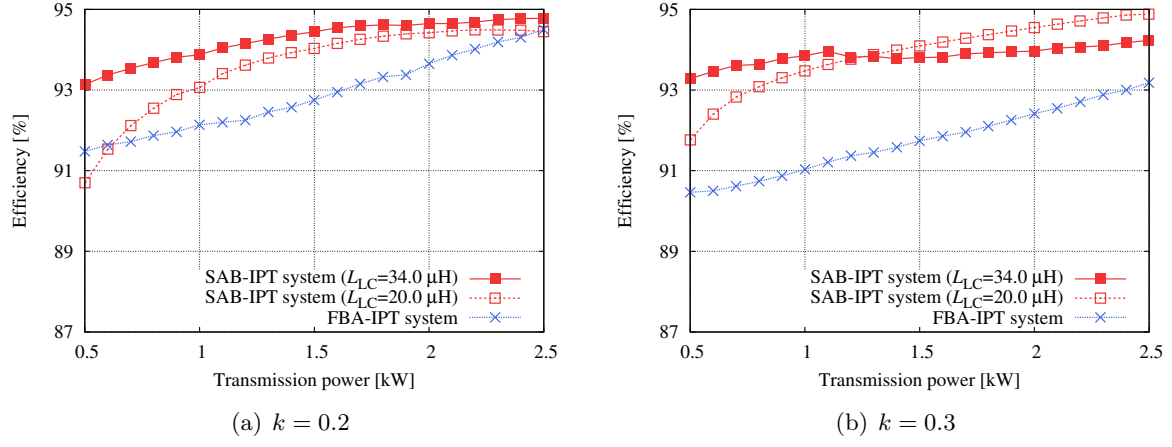


Fig. 6: Maximum efficiency characteristics of FBA/SAB-IPT systems controlled according to Fig. 5.

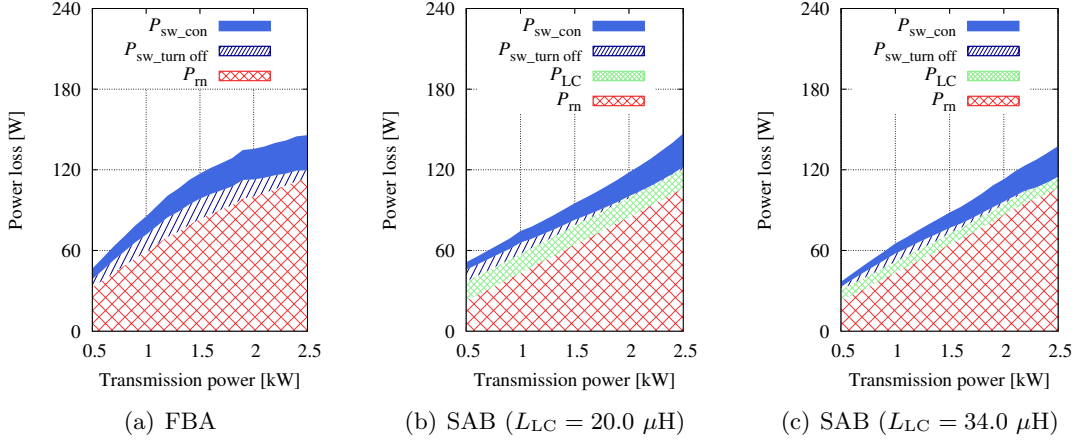


Fig. 7: Power-loss breakdown based on the theoretical analysis at $k = 0.2$.

system over a wide operation range. In addition, it can also be confirmed that the power loss P_{LC} in the LC circuit is small, especially with $L_{LC} = 34.0 \mu\text{H}$.

However, in Fig. 6(a), there are some points where the efficiency of the SAB-IPT system is slightly lower than that of the FBA-IPT system. When $P_{tr} = 2.5 \text{ kW}$, α_p and α_s in the FBA-IPT system are small, i.e., the reactive current to achieve soft switching is also small. In this case, the FBA-IPT system operates with relatively high efficiency. On the other hand, in the SAB-IPT system, a larger current is generated from the LC circuit than the necessity for soft switching. As a result, the efficiency of the SAB-IPT system (with $L_{LC} = 20.0 \mu\text{H}$) that uses a larger LC current is lower than that of the FBA-IPT system.

Here, the power loss in the LC circuit is constant regardless of the transmission power because the duty ratios of the legs and the DC source voltages are constant. Due to this, in the low power range, the ratio of P_{LC} to the whole system becomes high. As a result, the efficiency of the SAB-IPT system (with $L_{LC} = 20.0 \mu\text{H}$) that uses a larger LC current is lower than that of the FBA-IPT system. The above theoretical analysis shows that the SAB-IPT system is more efficient than the FBA-IPT system when L_{LC} can be properly designed.

Experiment

In the experiment, the switches in each system are operated with soft switching and controlled with open-loop based on the maximum-efficiency operation points shown in Fig. 5. Fig. 8 shows the output waveforms of the SAB converters at $k = 0.2$ and $P_{tr} = 2.5 \text{ kW}$ in the experiment.

From Fig. 8, it can be confirmed that these waveforms satisfy the soft-switching requirements in (14) and (15), and the soft-switching operation is achieved.

Next, Fig. 9 shows the maximum efficiency characteristics of FBA/SAB-IPT systems in the experiment. From Fig. 9, we can confirm that the SAB-IPT system is more efficient than the FBA-IPT system over wide operation range when $L_{LC} = 34.0 \mu\text{H}$. Especially, the efficiency at $k = 0.3$ and 2.5 kW is improved by 0.69 points, and the efficiency at $k = 0.2$ and 1.5 kW is improved by 0.88 points. Here, Fig. 10 shows the power-loss breakdown at $k = 0.2$ based on the measured current values. In Fig. 10, P_{rn} and P_{LC} are calculated using the measured current values and circuit parameters in Table II. In addition, “Other losses” represent the power loss subtracting P_{rn} and P_{LC} from the total power loss in the system. However, the power losses in the converters are dominant in the other losses. From Fig. 10, it is confirmed that the SAB-IPT system with $L_{LC} = 34.0 \mu\text{H}$ can reduce the whole-system loss over wide operation range.

On the other hand, the efficiency of the SAB-IPT system, even with $L_{LC} = 34.0 \mu\text{H}$, is lower than that of the FBA-IPT system by 0.24 points when $k = 0.2$, $P_{tr} = 2.5 \text{ kW}$. In a comparison of Figs. 7 and 10, it is confirmed that P_{rn} and P_{LC} in the experiment agree with these in the analysis. However, there is a large deviation in the power loss regarding the converter. This deviating causes different results from the theoretical analysis, and the SAB-IPT system is not more efficient than FBA-IPT system at the point. This problem can be improved by improving the power loss model of the converter and the design method for L_{LC} .

However, it can be confirmed that the tendency in Fig. 10 is close to the theoretical result in

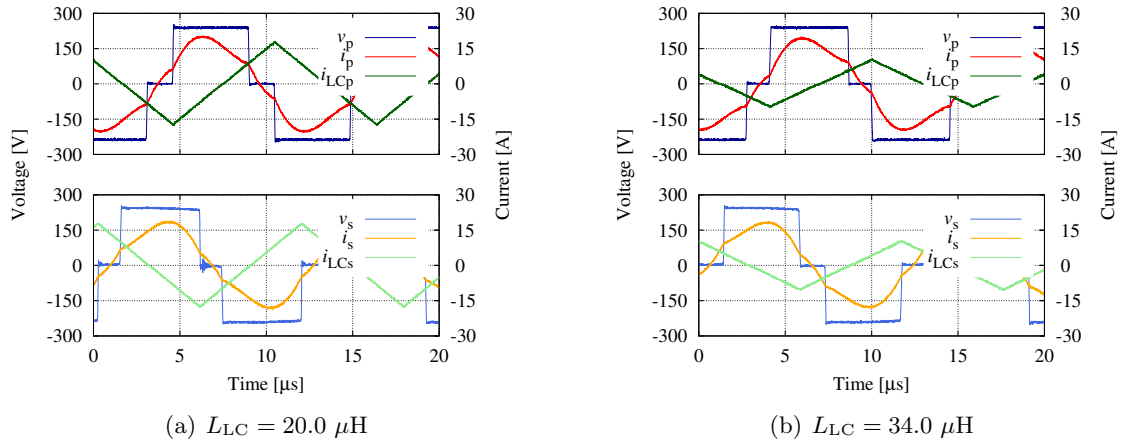


Fig. 8: Output waveforms of the SAB converters at $k = 0.2$ and $P_{tr} = 2.5 \text{ kW}$.

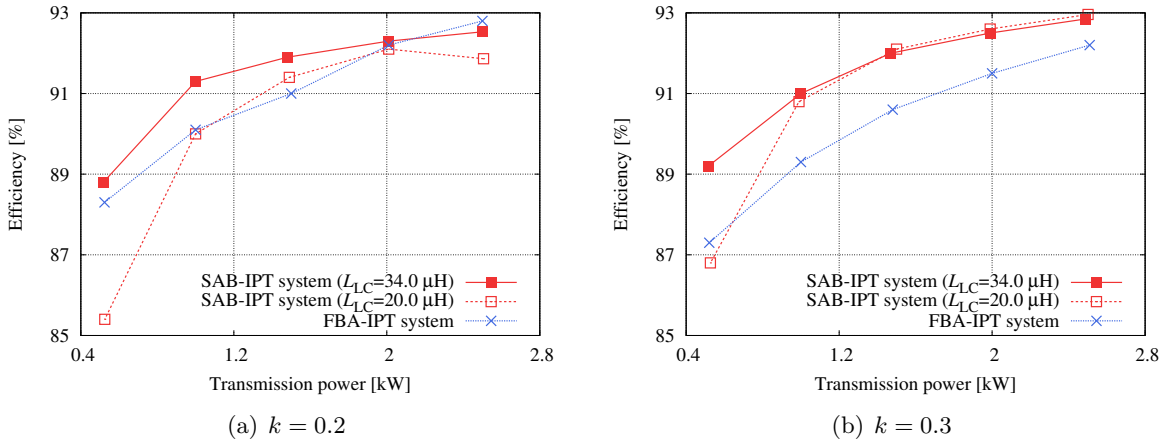


Fig. 9: Maximum efficiency characteristics of FBA/SAB-IPT systems in the experiment.

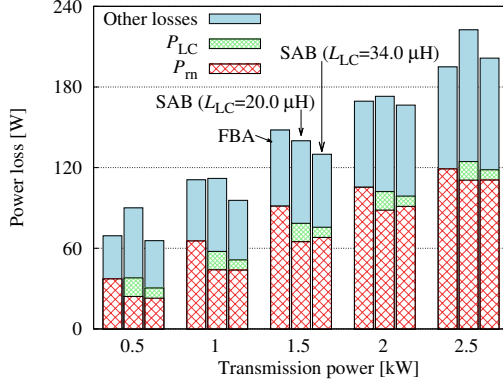


Fig. 10: Power-loss breakdown at $k = 0.2$ based on the measured current values.

Fig. 7, and it can be said that the theoretical analysis is valid. It can also be said that SAB-IPT system is also efficient when the double-sided LCC topology is applied.

Conclusion

This paper showed how to apply the SAB converter to IPT systems with the double-sided LCC topology. The theoretical analysis clarified the effect of the design of the LC circuit on the whole-system efficiency. As a result, regarding systems that are easy to maintain close coupling of the transmission coils, making L_{LC} small is an effective design for system efficiency. On the other hand, regarding the other system, making L_{LC} large is an effective design for system efficiency over a wide operation range.

In the experiment, the validities of the theoretical analysis result and the design guideline were evaluated by using two inductors L_{LC} ($20.0, 34.0 \mu\text{H}$). The SAB-IPT system could get higher efficiency over wide operation range as well as the theoretical analysis result. Especially, when $L_{LC} = 34.0 \mu\text{H}$, the efficiency at $k = 0.3$ and $P_{tr} = 2.5 \text{ kW}$ was improved by 0.69 points, and the efficiency at $k = 0.2$ and $P_{tr} = 1.5 \text{ kW}$ was improved by 0.88 points. However, in contrast to the result of the theoretical analysis, the efficiency of the SAB-IPT system at $k = 0.2$ and $P_{tr} = 2.5 \text{ kW}$ worsened by 0.24 points. To improve this problem, some improvements regarding the power loss model of the converter and the design method for L_{LC} are needed.

However, it was confirmed that the characteristics of the experimental result had a close tendency to that of the theoretical result, and it can be said that the theoretical analysis is valid. From the above, it can also be said that the SAB-IPT system has an effect when the double-sided LCC topology is applied. In future work, the power loss models and the design method for the LC circuit will be improved to achieve even higher efficiency.

Acknowledgment

The proposal for the SAB converter and the construction of the FBA converter are partially supported by JSPS KAKENHI Grant Number 20K14723. The proposal for the design guideline for the LC circuit to apply to the SAB converter with the double-sided LCC is partially supported by TEPCO Memorial Foundation.

References

- [1] H. Sumiya, E. Takahashi, N. Yamaguchi, K. Tani, S. Nagai, T. Fujita and H. Fujimoto, "Coil Scaling Law of Wireless Power Transfer Systems for Electromagnetic Field Leakage Evaluation for Electric Vehicles," *IEEJ Journal of Industry Applications*, vol. 10, no. 5, pp. 589–597, 2021.
- [2] H. Matsumoto, T. Zaitsu, R. Noborikawa, Y. Shibako and Y. Neba, "Control for Maximizing Efficiency of Three-Phase Wireless Power Transfer Systems At Misalignments," *IEEJ Journal of Industry Applications*, vol. 9, no. 4, pp. 401–407, 2020.
- [3] K. Nara, N. Madoiwa, K. Maeshiro and Y. Kaneko, "Wireless Power Transfer System with Ideal Transformer Characteristics Determined Solely by Coil Turns Ratio," *IEEJ Journal of Industry Applications*, vol. 9, no. 6, pp. 656–662, 2020.
- [4] B. Ji, K. Hata, T. Imura, Y. Hori, S. Shimada and O. Kawasaki, "Wireless Power Transfer System Design with Power Management Strategy Control for Lunar Rover," *IEEJ Journal of Industry Applications*, vol. 9, no. 4, pp. 392–400, 2020.
- [5] X. Zhang, T. Cai, S. Duan, H. Feng, H. Hu, J. Niu and C. Chen, "A Control Strategy for Efficiency Optimization and Wide ZVS Operation Range in Bidirectional Inductive Power Transfer System," *IEEE Transactions on Industrial Electronics*, vol. 66, no. 8, pp. 5958–5969, 2019.
- [6] R. Ota, D. J. Thrimawithana, U. K. Madawala and G. A. Covic, "Boundary of Soft-switching for Efficient Operation of Bi-directional IPT Systems," in *Proc. of 2020 IEEE PELS Work-shop on Emerging Technologies: Wireless Power Transfer (WoW)*, pp. 164–169, 2020.
- [7] R. Ota, D. S. Nugroho and N. Hoshi, "A consideration on maximum efficiency of resonant circuit of inductive power transfer system with soft-switching operation," *World Electr. Veh. J.*, vol. 10, no. 3, 2019.
- [8] G. R. Kalra, B. S. Riar, and D. J. Thrimawithana, "An integrated boost active bridge based secondary inductive power transfer converter," *IEEE Transactions on Power Electronics*, vol. 35, no. 12, pp. 12716–12727, 2020.
- [9] N. Fu, J. Deng, Z. Wang, W. Wang, and S. Wang, "A hybrid mode control strategy for lcc-lcc-compensated wpt system with wide zvs operation," *IEEE Transactions on Power Electronics*, vol. 37, no. 2, pp. 2449–2460, 2022.
- [10] R. Okada, R. Ota and N. Hoshi, "Novel Soft-switching Active-Bridge Converter for Bi-directional Inductive Power Transfer System," *IEEJ Journal of Industry Applications*, vol. 11, no. 1, pp. 97–107, 2022.
- [11] R. Ota and N. Hoshi, "Basic Study of Integrated On-board Converter for Dynamic WPT EV," in *Proc. of 5th International Electric Vehicle Technology Conference 2021*, 2021.
- [12] J. Zhang, Z. He, A. Luo, Y. Liu, G. Hu, X. Feng and L. Wang, "Total Harmonic Distortion and Output Current Optimization Method of Inductive Power Transfer System for Power Loss Reduction," *IEEE Access*, vol. 8, pp. 4724–4736, 2020.
- [13] R. Ota, D. S. Nugroho, and N. Hoshi, "A capacitance design guideline of snubber capacitors for soft switching in bi-directional inductive power transfer system considering battery charging cycle," in *Proc. of 2018 7th International Conference on Renewable Energy Research and Applications (ICRERA)*, 2018, pp. 1080–1085.